Materials Characterization 184 (2022) 111704

Contents lists available at ScienceDirect

Materials Characterization

journal homepage: www.elsevier.com/locate/matchar

Characterization of deformation-induced martensite with various AGSs upon Charpy impact loading and correlation with transformation mechanisms

Minghao Huang [a], Lingyu Wang [a], Chenchong Wang [a], Anna Mogucheva [b], Wei Xu [a,*]

[a] State Key Laboratory of Rolling and Automation, School of Materials Science and Engineering, Northeastern University, Shenyang 110819, China
[b] Laboratory of Mechanical Properties of Nanoscale Materials and Superalloys, Belgorod State University, Belgorod 308015, Russia

ARTICLE INFO

Keywords:
α'-martensite morphology
Grain size
Austenitic steel
Deformation-induced martensitic transformation

ABSTRACT

Deformation-induced martensitic transformation (DIMT) during quasi-static loading has drawn much attention in recent years since it is considered as one of the key strengthening mechanisms in advanced high-strength steels (AHSS). However, systematic investigations on martensitic transformation at high strain-rates are scarce due to difficulties in experimental designs. In this contribution, interrupted Charpy tests were used to study the transformation sequence of DIMT under high strain-rates ($\sim 10^2$–10^3 s^{-1}). Austenitic 321 stainless steel samples with increasing austenite grain sizes (AGSs) were designed to demonstrate the change in transformation sequence of α'-martensite and its morphology. Quasi-in-situ electron backscattered diffraction (EBSD) and selected transmission electron microscopy (TEM) experiments have revealed that, as the AGSs increases, the nucleation sites of α'-martensite change from austenite grain boundaries in ultra-fine-grained (UFG) samples to additional twin boundaries in fine-grained (FG) samples, and finally to ε-martensite in coarse-grained (CG) samples. Due to the spatial constraints imposed by different crystallographic boundaries, the morphology of transformed α'-martensite shifts from blocky in UFG samples to film-like in CG samples, with FG samples having a mixed morphology. It is found that the changed transformation sequence can be understood by considering the combined effect of stacking fault energy and twinning nucleation stress of austenite.

1. Introduction

The superior damage tolerance of austenitic steels facilitates their wide use in safety-critical applications, such as pressure vessels [1–4]. Compared with austenitic steels deforming under quasi-static loading conditions, the suppressed transformation-induced plastic (TRIP) effect of austenitic steels under dynamic loading conditions unfavorably limits the work hardening behavior and strength [5–8]. An in-depth study of deformation-induced martensitic transformation (DIMT) behavior under dynamic conditions is necessary to purposefully tailor the TRIP effect and optimize the work hardening rate. Basically, work hardening introduced by DIMT behavior is attributed to two aspects: a harder martensitic phase and the so-called dynamic Hall-Petch effect [9–11], which is related to the volume fraction of the α'-martensite phase and the morphology of α'-martensite. In previous studies, the evolution of the α'-martensite volume fraction during the loading condition has been systematically studied, and relevant phenomenology laws have been described [12–14]. To date, there has not been a clear relation and explanation of DIMT and the resulting morphology. However, the morphology of α'-martensite is believed to play a significant role in work hardening and crack propagation behavior [15,16]. Therefore, the relationship between the martensitic transformation sequences and α'-martensite morphology requires further study.

Crystallography shows that the morphology of α'-martensite is determined by the nucleation sites and the growth limitation boundaries. Thus, a detailed relationship between the martensitic transformation behavior and the morphology of α'-martensite is required. As previously stated, martensitic transformation is closely related to alloying [17–19] and AGSs [20,21]. Conventional alloying methods usually pose the problem of precipitation. Tailoring AGSs has been regarded as an effective method of microstructural control for the DIMT process without changing the chemical composition. Lee et al. [22,23] claimed that the width of stacking faults (SFs) decreases with a refinement of the AGSs on the crystallographic sites, which are the nucleation

* Corresponding author.
E-mail address: xuwei@ral.neu.edu.cn (W. Xu).

https://doi.org/10.1016/j.matchar.2021.111704
Received 10 November 2021; Received in revised form 20 December 2021; Accepted 21 December 2021
Available online 25 December 2021

Table 1
Chemical composition (wt%).

C	Si	Mn	Cr	P	S	Ni	N	Ti	Fe
0.021	0.578	1.384	17.56	0.033	0.0004	9.337	0.004	0.252	Balance

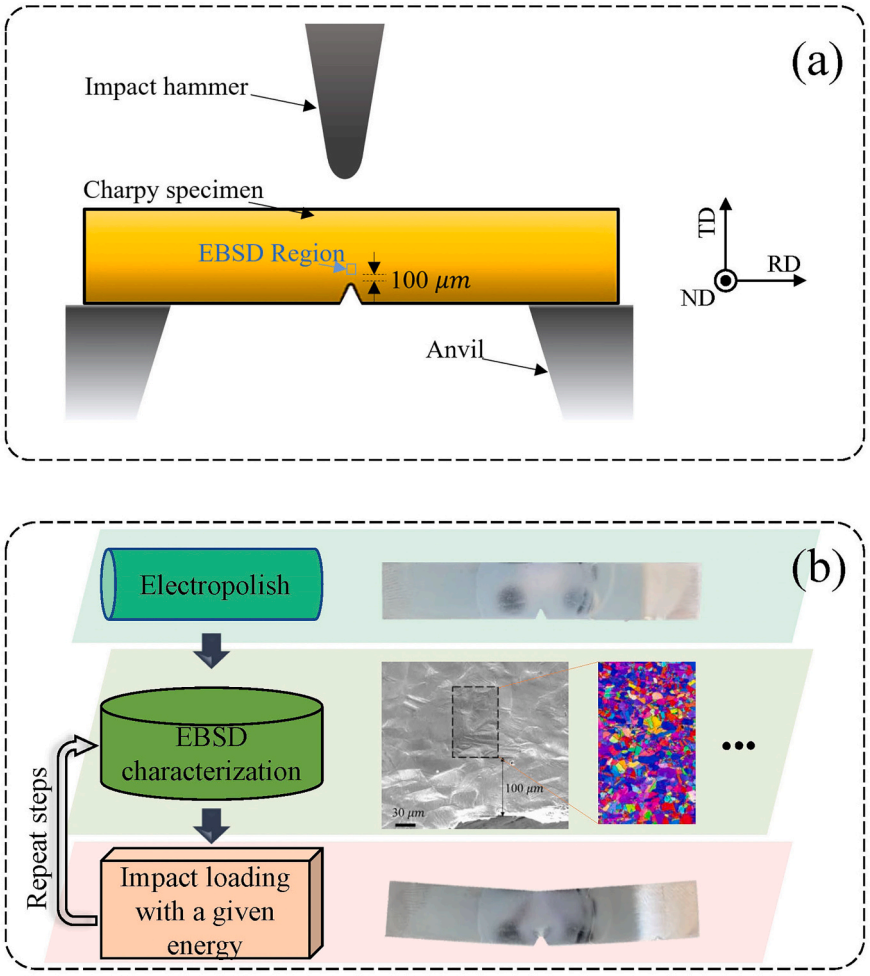

Fig. 1. Schematic diagram of the loading condition and EBSD characterization region. (a) Schematic illustration of the loading condition, (b) a flow chart of quasi-in-situ EBSD test during interrupted Charpy tests. RD, TD, and ND represent the rolling direction, transverse direction, and normal direction, respectively.

sites of twinning/ε-martensite. To easily determine the deformation mechanism of austenitic steel with various AGSs, 'apparent' stacking fault energy (SFE) is proposed [23]. With decreasing AGSs, which is phenomenon-based, the SFE value increases steadily. Furthermore, the effect of AGSs on the transition of the deformation mechanism has been extensively examined in various austenitic steels. With decreasing SFE, twinning, twinning+TRIP, and TRIP occur sequentially [24].

Therefore, in this study, austenitic steel with different grain sizes was fabricated to trigger the occurrence of different deformation mechanisms. And simultaneously evaluate the effect of AGSs on the morphology of α'-martensite. This research was ultimately aimed at determining the relations between martensitic transformation sequences and α'-martensite morphology. The mechanism described above could guide the tailoring of the deformation-induced α'-martensite (DIM) morphology, which affects both the strain hardening behavior and the propagation of cracks.

2. Experimental

2.1. Materials and test specimens

The selected metastable austenitic steel in this work was commercial AISI 321 plates with a 12 mm thickness. The chemical composition of the austenitic stainless steel is shown in Table 1. After repetitive cold rolling (65% in thickness reduction), a series annealing process (900 °C for 90 s, 900 °C for 30 min, and 1000 °C for 2 h) was conducted to obtain different grain sizes. Repetitive cold rolling resulted in sheets of 4.2 mm, which defines the upper limit of the specimen thickness. In addition, CG specimens exhibited some oxidation at the surface after the annealing treatment. Therefore, Charpy specimens were extracted from the center of 4.2 mm plates. To be consistent, all specimens were designed to have a thickness of 3 mm. The subsized 45°-V-notched Charpy impact samples used in the present study are 3 mm thick, 10 mm wide, and 55 mm long, and they were machined along the rolling direction of cold-rolled sheets (as shown in Fig. 1(a)).

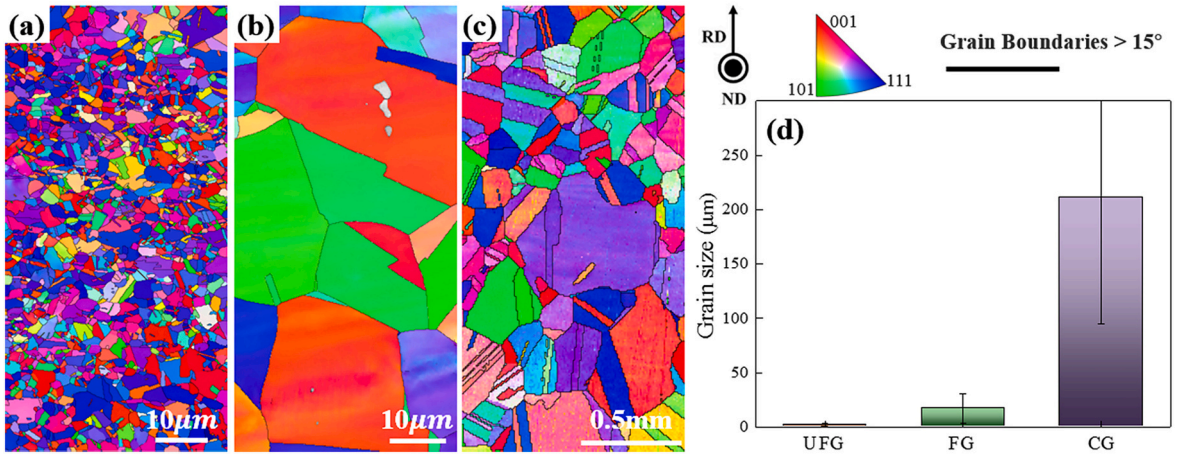

Fig. 2. SEM-EBSD IPF Z maps of specimens (a) ultrafine grains, (b) fine grains, (c) coarse grains, and (d) quantified AGSs of various specimens.

2.2. Microstructure and mechanical characterization

The microstructure of the specimens was characterized by a Zeiss Ultra field-emission scanning microscope (ZEISS, ULTRA 55) equipped with electron backscattered diffraction (EBSD; Oxford Instruments Aztec). For further characterization of the DIM, the UFG samples were also characterized using the transmission Kikuchi diffraction (TKD) technique, with a true spatial resolution of <10 nm. The EBSD/TKD results were processed using Oxford Instruments AztecCrystal 2.0 EBSD software. Transmission electron microscopy (TECNAI F20 TEM) was conducted to study the martensite nucleation behavior of UFG samples.

To observe the microstructure evolution, interrupted Charpy testing was conducted, the loading condition is schematically shown in Fig. 1 (a). For the loading tests, the Charpy impact tests used an MTS impact tester (SANS ZBC2452-C) with 1 J resolution, and the nominal strain was calculated based on the strain description by Li [25] under three-point bending conditions. In detail, the interrupted Charpy test was controlled by the given impact energy: 3 J, 6 J, and 9 J energy were used in the present study to induce 1.9%, 2.7%, and 3.5% nominal strains in the vicinity of the V-notch. For ease of microstructural characterization, a quasi-in-situ EBSD characterization has been carried out. The same region of the sample surface was scanned by EBSD during interrupted Charpy impact tests. This quasi-in-situ process is schematically shown in Fig. 1(b). The EBSD characterization focused on the root of the V-notch area (~100 μm near the root of the V-notch), as schematically illustrated in Fig. 1(b). Specimens for EBSD observation were electropolished before the loading tests. Thin foil specimens for TEM were prepared from the Charpy test specimens. The thin foils were jet-polished in a solution of 90% glacial acetic acid and 10% perchloric acid at −20 °C under 20 V.

2.3. Quantitation of apparent SFE values at various AGSs

AGSs are believed to play an important role in the deformation mechanism [26,27]. Previous studies have found that the overlapping SFs of austenite may be related to AGSs [28,29]. The SFE including the AGSs effect is called the 'apparent' SFE by J Y Lee [23]. The apparent SFE [26] values were calculated using the following equation:

$$\Gamma\left(mJ/m^2\right) = 2\rho_A\left(\Delta G_{Chem}^{fcc\to hcp} + \Delta G_{ex} + E^{strain}\right) + 2\sigma^{fcc/hcp} \quad (1)$$

where ρ_A is the density of atoms in a close packed plane given in moles per unit area, E^{strain} is the strain energy of the γ → ε transformation, and σ is the interfacial energy per unit area of the phase boundary between γ and ε. The chemical free energies of the transformation of austenite to ε-martensite ($\Delta G_{Chemfcc\to hcp}$) at various temperatures were calculated using ThermoCalc2017 software with the TCFE9 database. ΔG_{ex} is the excess free energy introduced by grain refinement of the γ phase. In the present study, ρ_A and σ were estimated to be 2.5 × 10^{-5} mol/m^2 and 27 × 10^{-3} J/m^2, respectively, and E^{strain} was assumed to be negligible [30]. The ΔG_{ex} value was calculated with the following equation [31], where d is the mean grain size of the original austenite (in μm).

$$\Delta G_{ex} = 170.06 \cdot exp(-d/18.55) \quad (2)$$

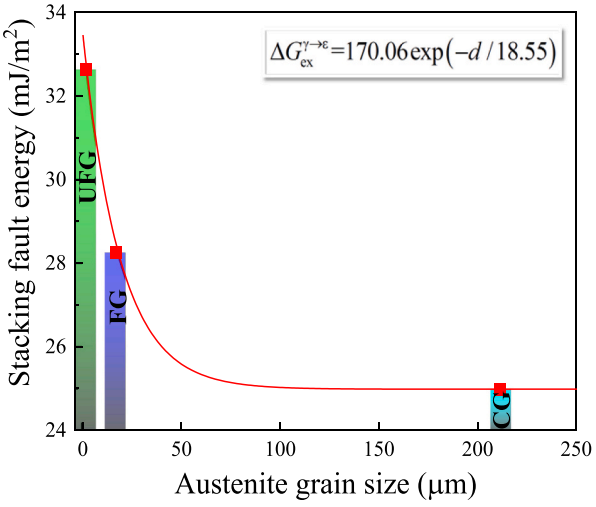

Fig. 3. Stacking fault energy (SFE) as a function of AGSs.

3. Results

3.1. Microstructure of specimens with various AGSs

Fig. 2(a–c) shows the inverse pole figure (IPF) microstructures of fabricated austenitic steel, and the mean AGSs of each specimen were statistically analyzed using AztecCrystal software, as presented in Fig. 2 (d). For ease of description, the steels were named ultrafine-grained (UFG), fine-grained (FG), and coarse-grained (CG). The mean AGSs of these specimens were determined to be 1.8 μm, 16.7 μm, and 211.3 μm. Meanwhile, the corresponding Charpy impact energy has been tested as 33.1±2.6 J, 42.4±3.3 J, and 45.1±0.1 J, respectively.

RD and ND refer to the rolling and normal directions, respectively.

The SFE of austenite is closely related to the grain size. As shown in Fig. 3, similar to previous studies [23,26,32], the calculated SFE value of the specimen first linearly decreases and then slowly decreases with increasing AGSs. For the CG, FG, and UFG samples, the corresponding

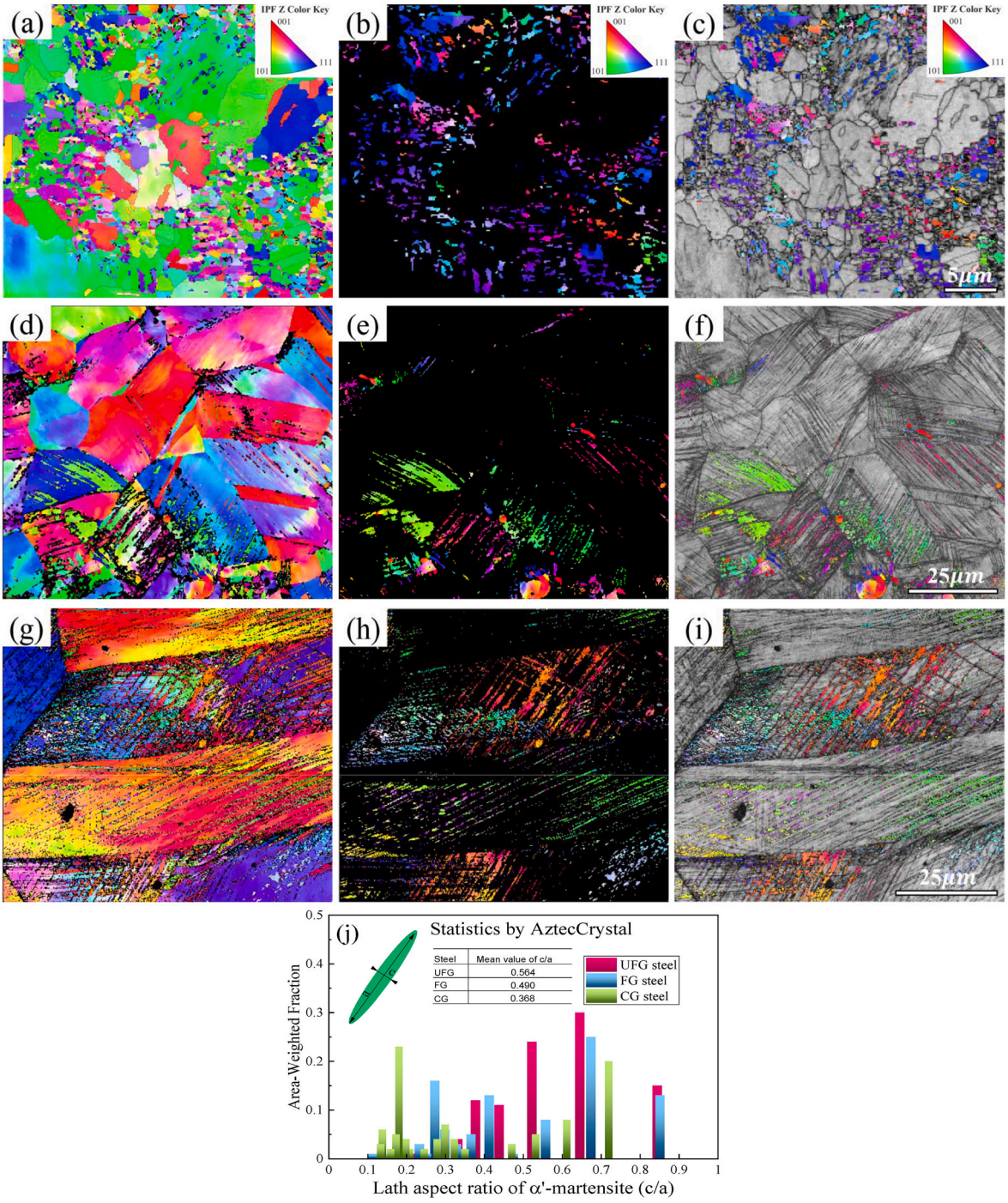

Fig. 4. Microstructure of steels after the Charpy test at 7.7% nominal strain.
(a)(d)(g) IPF Z maps of all phases for UFG, FG, and CG steel, respectively; (b)(e)(h) IPF Z maps of α'-martensite for UFG, FG, and CG steel, respectively; (c)(f))(i) band contrast and α'-martensite IPF Z for UFG, FG, and CG steel, respectively; (j) Lath aspect ratio (c/a) distributions for different AGSs.

SFE values were determined to be 24.9 mJ/m^2, 28.25 mJ/m^2, and 32.6 mJ/m^2, respectively.

3.2. Morphology of α'-martensite changes with AGSs

The morphology of deformation-induced α'-martensite as a function of various AGSs is shown in Fig. 4(a–i). Similar to a previous study on temperature-induced α'-martensite [33], the reduction in AGSs resulted in a smaller aspect ratio of α'-martensite. That is, in coarse austenite grains, α'-martensite is lath-like, whereas in ultrafine grains, it tends to develop into a round shape. To quantify the morphology of α'-martensite, Fig. 4(j) shows the distributions of the lath aspect ratio (c/a). The martensite structure of FG/CG steel exhibits a relatively lower c/a value. However, the higher c/a lath aspect ratio for UFG steel indicates that UFG steel shows more equiaxed α'-martensite.

In addition to the relations between AGSs and DIM morphology, the relations between the prior austenite grain size (PAGS) and morphology of α'-martensite have also been studied in martensitic steel. Casero et al. [34] built up the relations between PAGS and the morphology of temperature-induced α'-martensite in low-carbon steel. The reduction in PAGS resulted in blocky α'-martensite. Santofimia et al. [33] observed a similar phenomenon in 0.3C-1.6Si-3.5Mn (wt pct) steel. In summary, a

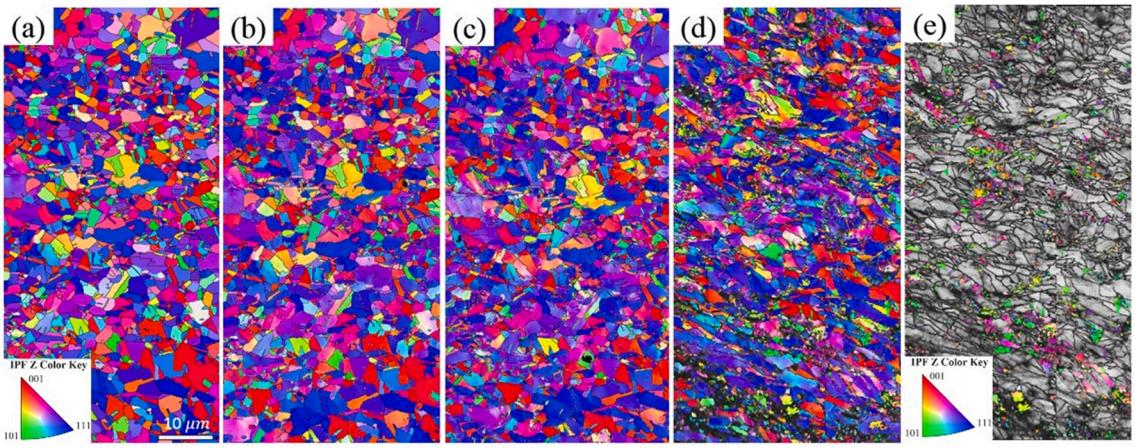

Fig. 5. Microstructure evolution of UFG steel during the Charpy test: colored face-centered cubic (fcc) phase IPF Z maps for (a) zero strain, (b) after 1.9% plastic deformation, (c) after 2.7% plastic deformation, and (d) after 3.5% plastic deformation; (e) colored bcc phase IPF Z maps for 3.5% plastic deformation. Quasi-in situ Charpy testing is performed in the impact tester. Red lines in the IPF Z map of (a), (b), and (c) represent twin boundaries. (For interpretation of the references to colour in this figure legend, the reader is referred to the web version of this article.)

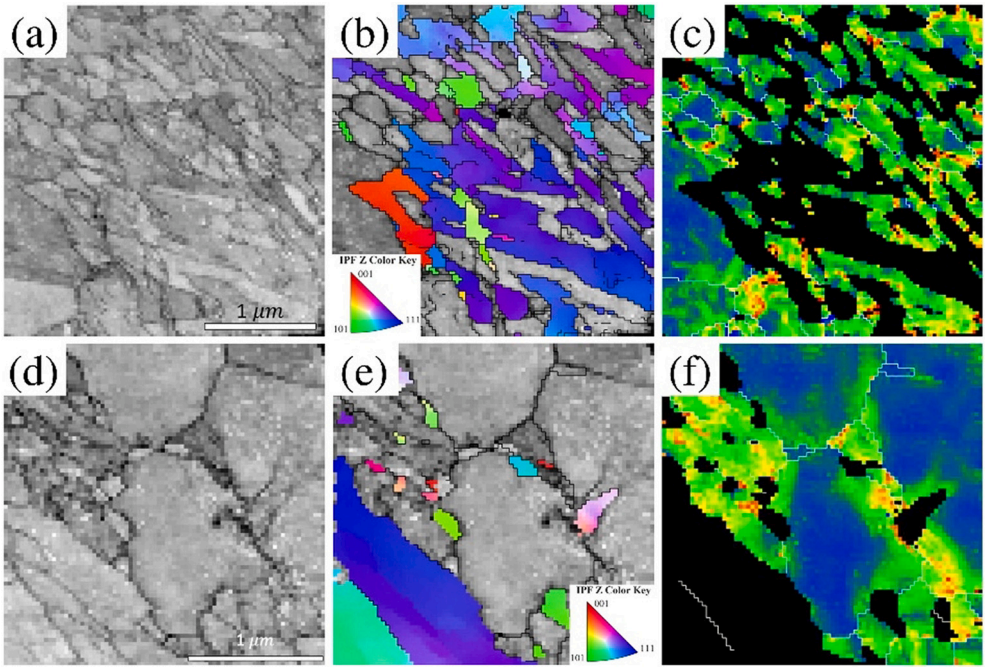

Fig. 6. Microstructure of UFG steel after the Charpy test at 3.5% nominal strain.
(a) and (d) band contrast map of all phases; (b) and (e) band contrast and α'-martensite IPF Z; (c) and (f) geometrically necessary dislocation (GND) map of austenite.

blocky α'-martensite is closely related to the smaller parent AGSs, despite the deformation/temperature induction.

Along with the effect on the aspect ratio, the number of variants per austenite grain is reduced as the AGSs are refined, as reflected in Fig. 4. Furuhara et al. [35] and Takaki et al. [36] observed a similar behavior; as the AGSs were reduced, the number of variants formed during martensitic transformation was reduced.

4. Discussion

4.1. Size-dependent martensitic transformation behaviors

As the main conclusion mentioned in the previous section, the morphology of α'-martensite changes substantially with varying AGSs. Therefore, the reason that AGSs influence the morphology of α'-martensite was further clarified from the crystallographic aspect. The nucleation and growth of α'-martensite were observed by quasi-in situ EBSD methods.

For UFG steel with blocky DIM only, the microstructure evolution during the Charpy impact test is shown in Fig. 5. In the range from 0 to 2.7% (Fig. 5(a–c)), no DIMT behavior occurred. Moreover, no deformation bands were detected, including hexagonal close-packed (hcp) or deformation twinning. However, the orientation of the austenite changes from a random orientation to an orientation close to (112), indicating the occurrence of double sliding. As the nominal strain further increases to ~3.5% (Fig. 5(d–e)), a significant amount of blocky α'-martensite forms, and the formed α'-martensite shows intense variant selection.

To examine the limited growth boundaries of α'-martensite and the microstructures of the UFG specimens, further characterization was

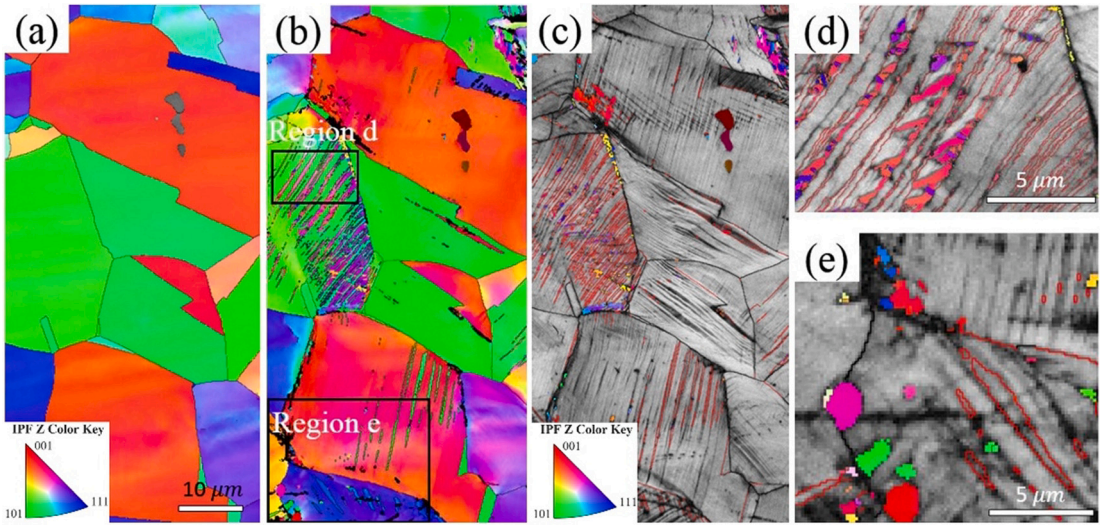

Fig. 7. Microstructural evolution of FG steel during the Charpy test. Colored fcc phase IPF Z maps for (a) zero strain, (b) after 1.9% plastic deformation, and (c) after 2.7% plastic deformation. Green bcc phase maps for (d) 2.7% plastic deformation, and (e) and (f) represent the magnified region of (d). Quasi-in situ Charpy testing is performed in the impact tester. Red lines in the IPF Z map of (d) and (e) represent twin boundaries. (For interpretation of the references to colour in this figure legend, the reader is referred to the web version of this article.)

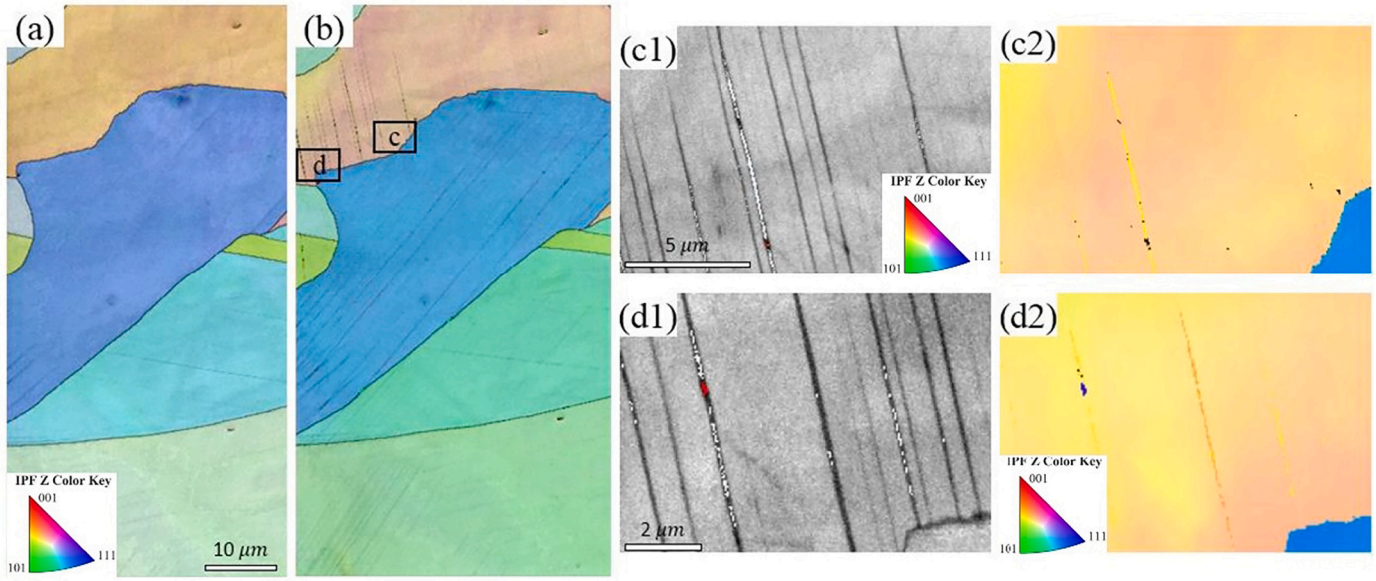

Fig. 8. Combined EBSD image quality and IPF for the microstructural evolution of CG steel via the Charpy test. Colored fcc phase IPF Z maps for (a) zero strain and (b) after 1.9% plastic deformation. (c1) and (d1) α'-martensite, phase map of regions c and d, and (d) after 1.9% plastic deformation; colored bcc phase IPF Z maps for 1.9% plastic deformation. Quasi-in situ Charpy testing is performed in the impact tester.

carried out through TKD methods (Fig. 6). TKD sampling was conducted beneath the V-notch of the tested samples, and TKD maps were collected using step sizes of 5 nm. Based on the calculated SFE results, deformation twinning is believed to occur in UFG steel. However, no mechanical twins were observed in the UFG specimen strained by 3.5% (Fig. 6). It was found that grain refinement down to the UFG scale leads to abnormal nucleation of α'-martensite compared with our previous studies [37,38]. That is, as shown in Fig. 6(b and e), α'-martensite seems to nucleate at austenite grain boundaries.

For FG steel, both lath-like and blocky α'-martensite formed during the Charpy tests. Thus, a similar in situ EBSD test is conducted in FG steel, as shown in Fig. 7. With increasing nominal strain, a significant amount of deformation twinning and α'-martensite forms (Fig. 7(b and c)).

As presented in Fig. 7(d and e), the microstructure of FG steel under 1.9% nominal strain shows that α'-martensite nucleates at twin boundaries and grain boundaries. For α'-martensite nucleation inside the deformation twinning boundaries, its growth is limited, leading to lath-like α'-martensite (Fig. 7(d)). However, α'-martensite nucleation at the grain boundaries is mainly limited by the grain boundaries, which finally grows to blocky-sized α'-martensite (Fig. 7(e)). The growth limit boundaries, i.e., grain and twinning boundaries, facilitate blocky and lath-like α'-martensite formation, respectively.

Similarly, the microstructural evolution of CG steel has also been characterized (Fig. 8). EBSD maps of 1.9% strained CG steel are shown in Fig. 8(b). The α'-martensite nucleates inside ε-martensite plates and grows in ε-martensite plates, and the growth of α'-martensite is limited by γ/ε phase boundaries [19]. For deformation-induced α'-martensite formation, the presence of ε-martensite provides nucleation sites with a lower chemical driving force, as previously illustrated by Olson [39].

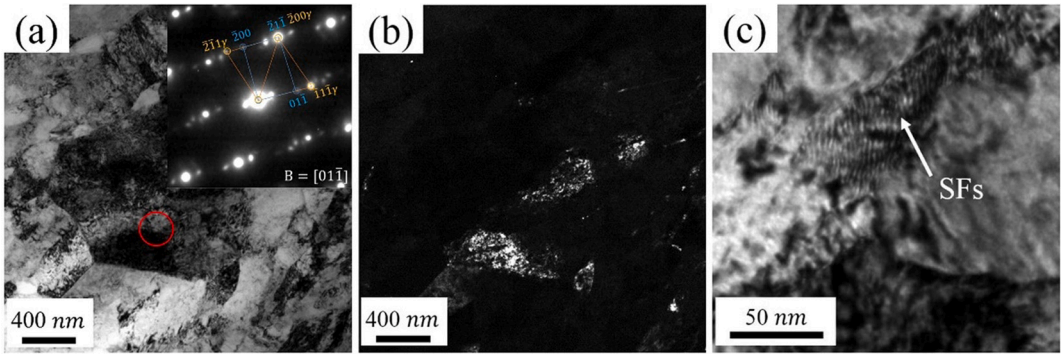

Fig. 9. TEM microscopy of the phase transformation behaviors in UFG steel: (a) bright-field images of α'-martensite nucleation at grain boundaries; (b) corresponding dark-field images of the red cycle; and (c) bright-field images of austenite grains full of SFs. (For interpretation of the references to colour in this figure legend, the reader is referred to the web version of this article.)

Thus, the deformation primarily induces α'-martensite and only nucleates at the ε phase. On the growth site, more importantly, the γ/ε phase boundaries act as insuperable barriers that hinder the growth of deformation-induced α'-martensite [30]. As shown in Fig. 8(c1 and d1), α'-martensite growth was limited, and the morphology of ε-martensite was finally maintained, i.e., lath-like.

4.2. An in-depth study of the abnormal martensitic transformation behavior of UFG steel

According to the aforementioned phenomenon, the absence of deformation bands, i.e., ε-martensite and deformation twinning, is responsible for the formation of blocky α'-martensite in UFG steel. Thus, the reasons for the absence of deformation bands need further discussion.

To initiate discussion of the absence of deformation bands, it is important to first study the absence of ε-martensite. The suppressed ε-martensite formation can be explained by the relatively high SFE. As calculated in Fig. 3, when the AGSs decrease to UFG, the SFE reaches ~33 mJ/m^2, which is beyond the range of ε-martensite formation based on Hofmann et al. [40,41]. Thus, for UFG steel, the formation of ε-martensite would not exist.

Conversely, the calculated SFE ranges from 20 mJ/m^2 to 40 mJ/m^2, which indicates that deformation twinning (TWIP) would occur in UFG steel [41]. However, the experimental evidence demonstrates the opposite results. This behavior cannot be explained by the SFE only. Instead, twinning stress is taken into consideration, which is defined as the stress required to generate twinning. K.M. Rahman et al. [42–45] proposed a phenomenological relationship between the AGSs and twinning stress, where the twin nucleation stress increases with decreasing grain size following a Hall–Petch type relationship. Furthermore, from a crystallographic perspective, El-Danaf et al. [46] found that twinning stress is expected to increase with grain refinement since the slip length and dislocation density is reduced, thus making twin nucleation more difficult. The models of Mahajan and Chin et al. [47] and M. M. Wang et al. [48] explain that the nucleation of deformation twins is related to stacking fault pairs and Shockley partial dislocations, and they conclude that a higher nominal twinning stress is required for the onset of twinning in smaller grains. For the present studied UFG steel, before the applied stress achieved twinning stress, DIMT occurred. Thus, extremely small AGSs imply no deformation band formation, but α'-martensite transformation occurred.

This size effect associated with α'-martensite transformation, as described herein, is consistent with earlier findings [48,49]. As reflected in the TEM results (Fig. 9), the formation of SFs and dislocations facilitates the onset of α'-martensite transformation.

The results indicate that grain size refinement limits the formation of deformation bands and then induces blocky α'-martensite. Additionally,

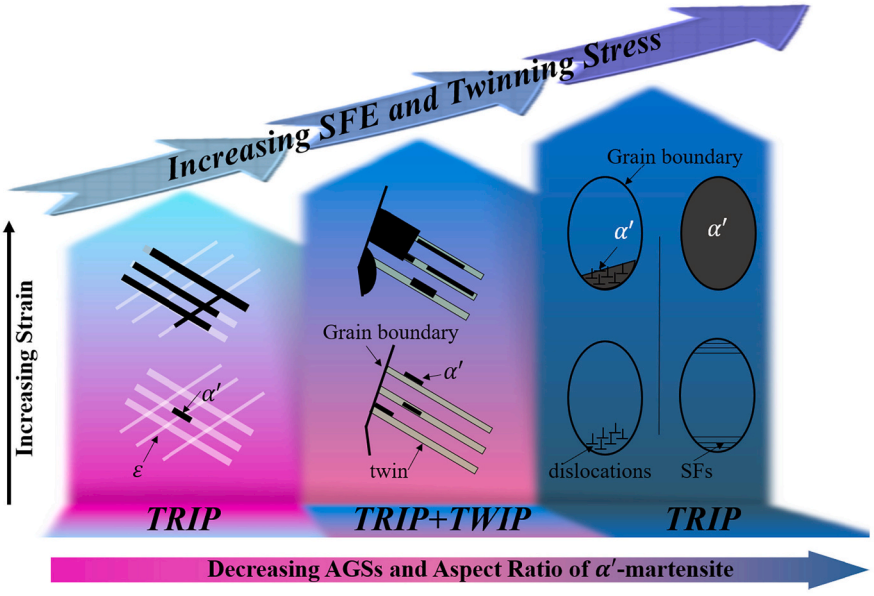

Fig. 10. Schematic sketch of the size-dependent transformation behaviors and morphology of α'-martensite under the Charpy impact test.

we reveal that size effects should be taken into deep consideration; to some extent, smaller particles are less mechanically stable.

4.3. Relationship between the AGSs and morphology of α'-martensite

The morphology of α'-martensite was determined to be closely related to the martensitic transformation sequences. This finding draws attention to the nucleation and growth of α'-martensite of various AGSs. The scheme in Fig. 10 shows the morphology of α'-martensite and martensitic transformation sequences as a function of the AGSs. Based on the microstructural evolution in Fig. 8, the SFE of SUS321 steel with extremely large grain sizes (CG steel) is situated within the deformation mechanism of the TRIP.

γ → ε-martensite→α'-martensite transformation sequences were triggered in CG steel, and film-like α'-martensite was found in Fig. 8. As the grain size decreases to FG, by increasing the SFE to ~30 mJ/m^2, pronounced twinning formation can be observed, as shown in Fig. 7. Both TWIP and TRIP behaviors are found. The α'-martensite limited by twinning boundaries finally results in a lath-like α'-martensite, but the α'-martensite limited by the grain boundaries grows into a blocky size. As the grain size further decreases to UFG, both the SFE and twinning stress exponentially increase. The formation of deformation twinning is intensely suppressed, leading to an abnormal TRIP effect, where α'-martensite may nucleate at grain boundaries/SFs and result in a blocky α'-martensite. Additionally, the present results enable the optimization of the rational microstructural design of austenitic steels involving the formation of a controlled morphology of α'-martensite.

5. Conclusions

The relationship between DIM morphology and AGSs was thoroughly investigated under dynamic loading conditions. The DIM at large strains exhibits various aspect ratios and its morphology is controlled by growth limitations at different boundaries. The following conclusions can be drawn from the investigation:

1. As the AGS increases, the deformation products of metastable austenite consist of α'-martensite alone (UFG samples), twinning+α'-martensite (FG samples), and α'-martensite/ε-martensite (CG samples). At large strains, most intermediate deformation products (i.e., deformation twins and ε-martensite) will further transform into α'-martensite.
2. It is found that the morphology of α'-martensite is controlled by its nucleation sites and adjacent crystallographic/phase boundaries. If α'-martensite is nucleated within deformation twins or existing ε-martensite (FG and CG samples), twin boundaries and γ-ε boundaries are shown to stop the growth of α'-martensite, resulting in lath-like α'-martensite. In the absence of twins and ε-martensite (UFG samples), α'-martensite nucleates at austenite grain boundaries and is constrained by austenite boundaries on the other side of the nucleate, promoting the formation of blocky α'-martensite. When both twin boundaries and austenite boundaries are present, a mix of lath-like and blocky morphologies are found in FG samples.
3. The absence of deformation twins and ε-martensite in UFG steels is attributed to the combined effect of twining nucleation stress and SFE. With decreasing AGSs, the twinning nucleation stress and SFE increase, resulting in higher activation energies for twins and ε-martensite and their suppression during transformation.

Data availability statement

The raw data required to reproduce these findings are available upon reasonable request.

Declaration of Competing Interest

The authors declare no competing financial interests.

Acknowledgements

The research was financially supported by the National Natural Science Foundation of China (No. U1808208, and 51961130389), and International/Regional Cooperation and Exchange Program of NSFC (NSFC-RFBR, No. 52011530032).

References

[1] H. Wang, J. Zhou, Y. Luo, P. Tang, Y. Chen, Forming of ellipse heads of large-scale austenitic stainless steel pressure vessel, Procedia Eng. 81 (2014) 837–842, https://doi.org/10.1016/j.proeng.2014.10.085.
[2] M.C. Fonseca, I.N. Bastos, E. Baggio-Saitovitch, D. Sánchez, Characterization of oxides of stainless steel UNS S30400 formed in offshore environment, Corros. Sci. 55 (2012) 34–39, https://doi.org/10.1016/j.corsci.2011.09.029.
[3] J.K. Ren, Q.Y. Chen, J. Chen, Z.Y. Liu, Enhancing strength and cryogenic toughness of high manganese TWIP steel plate by double strengthened structure design, Mater. Sci. Eng. A 786 (2020), 139397, https://doi.org/10.1016/j.msea.2020.139397.
[4] J. Chen, J.K. Ren, Z.Y. Liu, G.D. Wang, The essential role of niobium in high manganese austenitic steel for application in liquefied natural gas tanks, Mater. Sci. Eng. A 772 (2020), 138733, https://doi.org/10.1016/j.msea.2019.138733.
[5] P. Xia, F.J.C. Rodríguez, I. Sabirov, Microstructure evolution and adiabatic heating during dynamic biaxial deformation of a 304 stainless steel, Mater. Sci. Eng. A 793 (2020), 139829, https://doi.org/10.1016/j.msea.2020.139829.
[6] Y.F. Shen, X.X. Li, X. Sun, Y.D. Wang, L. Zuo, Twinning and martensite in a 304 austenitic stainless steel, Mater. Sci. Eng. A 552 (2012) 514–522, https://doi.org/10.1016/j.msea.2012.05.080.
[7] J. Talonen, H. Hänninen, Formation of shear bands and strain-induced martensite during plastic deformation of metastable austenitic stainless steels, Acta Mater. 55 (2007) 6108–6118, https://doi.org/10.1016/j.actamat.2007.07.015.
[8] X. Wei, R. Fu, L. Li, Tensile deformation behavior of cold-rolled TRIP-aided steels over large range of strain rates, Mater. Sci. Eng. A 465 (2007) 260–266, https://doi.org/10.1016/j.msea.2007.02.126.
[9] H.K. Yeddu, Phase-field modeling of austenite grain size effect on martensitic transformation in stainless steels, Comput. Mater. Sci. 154 (2018) 75–83, https://doi.org/10.1016/j.commatsci.2018.07.040.
[10] A. Perlade, O. Bouaziz, Q. Furnémont, A physically based model for TRIP-aided carbon steels behaviour, Mater. Sci. Eng. A 356 (2003) 145–152, https://doi.org/10.1016/S0921-5093(03)00121-7.
[11] I.R.S. Filho, A. Dutta, D.R.A. Junior, W. Lu, M.J.R. Sandim, D. Ponge, H.R. Z. Sandim, D. Raabe, The impact of grain-scale strain localization on strain hardening of a high-Mn steel: real-time tracking of the transition from the γ→ε→α' transformation to twinning, Acta Mater. 197 (2020) 123–136, https://doi.org/10.1016/j.actamat.2020.07.038.
[12] M.J. Sohrabi, M. Naghizadeh, H. Mirzadeh, Deformation-induced martensite in austenitic stainless steels: a review, Arch. Civil Mech. Eng. 124 (2020) 1–24, https://doi.org/10.1007/s43452-020-00130-1.
[13] M. Soleimani, A. Kalhor, H. Mirzadeh, Transformation-induced plasticity (TRIP) in advanced steels: a review, Mater. Sci. Eng. A 795 (2020) 140023.1–140023.14, https://doi.org/10.1016/j.msea.2020.140023.
[14] Z. Dai, H. Chen, R. Ding, Q. Lu, C. Zhang, Z. Yang, S.V.D. Zwaag, Fundamentals and application of solid-state phase transformations for advanced high strength steels containing metastable retained austenite, Mater. Sci. Eng. R. Rep. 143 (2021) 1–39, https://doi.org/10.1016/j.mser.2020.100590.
[15] K.T. Faber, A.G. Evans, Crack deflection process—I. theory, and II. Experiment, Acta Metall. 31 (1983) 565–576, https://doi.org/10.1016/0001-6160(83)90046-9.
[16] Z. Szaraz, P. Haehner, J. Straska, S. Ripplinger, Effect of phase separation on tensile and Charpy impact properties of MA956 ODS steel, Mater. Sci. Eng. A 700 (2017) 425–437, https://doi.org/10.1016/j.msea.2017.06.010.
[17] M.C. Jo, M.C. Jo, A. Zargaran, S.S. Sohn, N.J. Kim, S. Lee, Effects of Al addition on tensile properties of partially recrystallized austenitic TRIP/TWIP steels, Mater. Sci. Eng. A 806 (2021), 140823, https://doi.org/10.1016/j.msea.2021.140823.
[18] C. Quitzke, C. Schrder, C. Ullrich, M. Mandel, M. Wendler, Evaluation of strain-induced Martensite formation and mechanical properties in N-alloyed austenitic stainless steels by in situ tensile tests, Mater. Sci. Eng. A 808 (2021), 140930, https://doi.org/10.1016/j.msea.2021.140930.
[19] N. Saenarjhan, J.H. Kang, S.J. Kim, Effects of carbon and nitrogen on austenite stability and tensile deformation behavior of 15Cr-15Mn-4Ni based austenitic stainless steels, Mater. Sci. Eng. A 742 (2019) 608–616, https://doi.org/10.1016/j.msea.2018.11.048.
[20] X. Pan, S. Shen, C. Wu, J. Li, J. Chen, Unusual relationship between impact toughness and grain size in a high-manganese steel, J. Mater. Sci. Technol. 89 (2021) 122–132, https://doi.org/10.1016/j.jmst.2021.01.089.
[21] Y.Z. Tian, Y. Bai, L.J. Zhao, S. Gao, H.K. Yang, A. Shibata, Z.F. Zhang, N. Tsuji, A novel ultrafine-grained Fe-22Mn-0.6C TWIP steel with superior strength and

ductility, Mater. Charact. 126 (2017) 74–80, https://doi.org/10.1016/j.matchar.2016.12.026.
[22] M.G. Farahani, A.Z. Hanzaki, H.R. Abedi, J.H. Kim, L.P. Karjalainen, On the activation of alternated stacking fault pair twinning mechanism in a very large-grained Fe–29Mn–2.4Al steel, Scr. Mater. 178 (2020) 301–306, https://doi.org/10.1016/j.scriptamat.2019.11.035.
[23] J.Y. Lee, J.S. Hong, S.H. Kang, Y.K. Lee, The effect of austenite grain size on deformation mechanism of Fe-17Mn steel, Mater. Sci. Eng. A 809 (2021), 140972, https://doi.org/10.1016/j.msea.2021.140972.
[24] H. Gwon, H.K. Ji, J.K. Kim, D.W. Suha, S.J. Kim, Role of grain size on deformation microstructures and stretch-flangeability of TWIP steel, Mater. Sci. Eng. A 773 (2020), 138861, https://doi.org/10.1016/j.msea.2019.138861.
[25] L. Jin, J. Dong, J. Sun, A.A. Luo, In-situ investigation on the microstructure evolution and plasticity of two magnesium alloys during three-point bending, Int. J. Plast. 72 (2015) 218–232, https://doi.org/10.1016/j.ijplas.2015.05.010.
[26] X. Li, L. Chen, Y. Zha, X. Yuan, R.D.K. Misra, Influence of original austenite grain size on tensile properties of a high-manganese transformation-induced plasticity (TRIP) steel, Mater. Sci. Eng. A 715 (2018) 257–265, https://doi.org/10.1016/j.msea.2017.12.107.
[27] O.A. Zambrano, Stacking fault energy maps of Fe–Mn–Al–C–Si steels: effect of temperature, grain size, and variations in compositions, J. Eng. Mater. Technol. 138 (2016), 041010, https://doi.org/10.1115/1.4033632.
[28] B.H. Jiang, L. Sun, R. Li, T.Y. Hsu, Influence of austenite grain size on γ-ε martensitic transformation temperature in Fe-Mn-Si-Cr alloys, Scr. Metall. Mater. 33 (1995) 63–68, https://doi.org/10.1016/0956-716X(95)00081-6.
[29] J. Chen, F.T. Dong, Z.Y. Liu, G.D. Wang, Grain size dependence of twinning behaviors and resultant cryogenic impact toughness in high manganese austenitic steel, J. Mater. Res. Technol. 10 (2021) 175–187, https://doi.org/10.1016/j.jmrt.2020.12.030.
[30] T. Masumura, N. Nakada, T. Tsuchiyama, S. Takaki, T. Koyano, K. Adachi, The difference in thermal and mechanical stabilities of austenite between carbon- and nitrogen-added metastable austenitic stainless steels, Acta Mater. 84 (2015) 330–338, https://doi.org/10.1016/j.actamat.2014.10.041.
[31] Y.K. Lee, C. Choi, Driving force for γ→ε martensitic transformation and stacking fault energy of γ in Fe-Mn binary system, Metall. Mater. Trans. A 31 (2000) 355–360, https://doi.org/10.1007/s11661-000-0271-3.
[32] S.I. Lee, S.Y. Lee, J. Han, B. Hwang, Deformation behavior and tensile properties of an austenitic Fe-24Mn-4Cr-0.5C high-manganese steel: effect of grain size, Mater. Sci. Eng. A 742 (2019) 334–343, https://doi.org/10.1016/j.msea.2018.10.107.
[33] J. Hidalgo, M.J. Santofimia, Effect of prior austenite grain size refinement by thermal cycling on the microstructural features of as-quenched lath Martensite, Metall. Mater. Trans. A 47 (2016) 5288–5301, https://doi.org/10.1007/s11661-016-3525-4.
[34] C.C. Casero, J. Sietsma, M.J. Santofimia, The role of the austenite grain size in the martensitic transformation in low carbon steels, Mater. Des. 167 (2019), 107625, https://doi.org/10.1016/j.matdes.2019.107625.
[35] T. Furuhara, K. Kikumoto, H. Saito, T. Sekine, T. Ogawa, S. Morito, T. Maki, Phase transformation from fine-grained austenite, ISIJ Int. 48 (2008) 1038–1045, https://doi.org/10.2355/isijinternational.48.1038.
[36] S. Takaki, K. Fukunaga, J. Syarif, T. Tsuchiyama, Effect of grain refinement on thermal stability of metastable austenitic steel, Mater. Trans. 45 (2004) 2245–2251, https://doi.org/10.2320/matertrans.45.2245.
[37] J. Wang, M. Huang, J. Hu, C. Wang, W. Xu, EBSD investigation of the crystallographic features of deformation-induced martensite in stainless steel, J. Mater. Sci. Technol. 69 (2021) 148–155, https://doi.org/10.1016/j.jmst.2020.08.023.
[38] J.L. Wang, M.H. Huang, X.H. Xi, C.C. Wang, W. Xu, Characteristics of nucleation and transformation sequence in deformation-induced martensitic transformation, Mater. Charact. 163 (2020), 110234, https://doi.org/10.1016/j.matchar.2020.110234.
[39] G.B. Olson, M. Cohen, A mechanism for the strain-induced nucleation of martensitic transformations, J. Less Common Metals 28 (1972) 107–118, https://doi.org/10.1016/0022-5088(72)90173-7.
[40] O. Grässel, G. Frommeyer, C. Derder, H. Hofmann, Phase transformations and mechanical properties of Fe-Mn-Si-Al TRIP-steels, J. Phys. IV France 07 (1997) 383–388, https://doi.org/10.1051/jp4:1997560.
[41] K. Sato, M. Ichinose, Y. Hirotsu, Y. Inoue, Effects of deformation induced phase transformation and twinning on the mechanical properties of austenitic Fe–Mn–Al alloys, ISIJ Int. 52 (2007) 868–877, https://doi.org/10.2355/isijinternational.29.868.
[42] K.M. Rahman, V.A. Vorontsov, D. Dye, The effect of grain size on the twin initiation stress in a TWIP steel, Acta Mater. 89 (2015) 247–257, https://doi.org/10.1016/j.actamat.2015.02.008.
[43] M.A. Meyers, U.R. Andrade, A.H. Chokshi, The effect of grain size on the high-strain, high-strain-rate behavior of copper, Metall. Mater. Trans. A 26 (1995) 2881–2893, https://doi.org/10.1007/BF02669646.
[44] A.M. Meyers, O. Vöhringer, A.V. Lubarda, The onset of twinning in metals: a constitutive description, Acta Mater. 49 (2001) 4025–4039, https://doi.org/10.1016/S1359-6454(01)00300-7.
[45] R. Ueji, N. Tsuchida, D. Terada, N. Tsuji, Y. Tannaka, A. Takemura, K. Kunishige, Tensile properties and twinning behavior of high manganese austenitic steel with fine-grained structure, Scr. Mater. 59 (2008) 963–966, https://doi.org/10.1016/j.scriptamat.2008.06.050.
[46] E.E. Danaf, S.R. Kalidindi, R.D. Doherty, Influence of grain size and stacking-fault energy on deformation twinning in fcc metals, Metall. Mater. Trans. A 30 (1999) 1223–1233, https://doi.org/10.1007/s11661-999-0272-9.
[47] S. Mahajan, G.Y. Chin, Formation of deformation twins in f.c.c. crystals, Acta Metall. 21 (1973) 1353–1363, https://doi.org/10.1016/0001-6160(73)90085-0.
[48] M.M. Wang, C.C. Tasan, D. Ponge, A. Kostka, D. Raabe, Smaller is less stable: size effects on twinning vs. transformation of reverted austenite in TRIP-maraging steels, Acta Mater. 79 (2014) 268–281, https://doi.org/10.1016/j.actamat.2014.07.020.
[49] Y. Matsuoka, T. Iwasaki, N. Nakada, T. Tsuchiyama, S. Takaki, Effect of grain size on thermal and mechanical stability of austenite in metastable austenitic stainless steel, ISIJ Int. 53 (2013) 1224–1230, https://doi.org/10.2355/isijinternational.53.1224.